

Apatite trace element composition as an indicator of ore deposit types: A machine learning approach

KUN-FENG QIU^{1,*}, TONG ZHOU¹, DAVID CHEW², ZHAO-LIANG HOU³, AXEL MÜLLER^{4,5},
HAO-CHENG YU¹, ROBERT G. LEE⁶, HUAN CHEN⁷, AND JUN DENG^{1,8,*}

¹Frontiers Science Center for Deep-time Digital Earth, State Key Laboratory of Geological Processes and Mineral Resources, School of Earth Sciences and Resources, China University of Geosciences, Beijing 100083, China

²Department of Geology, School of Natural Sciences, Trinity College Dublin, Dublin 2, Ireland

³Department of Geology, University of Vienna, Vienna 1090, Austria

⁴Natural History Museum, University of Oslo, Oslo 0562, Norway

⁵Natural History Museum, London SW7 5BD, U.K.

⁶Mineral Deposit Research Unit (MRDU), The University of British Columbia, Main Mall, Vancouver, British Columbia V6T 1Z4, Canada

⁷Institute of Marine Geology, College of Oceanography, Hohai University, Nanjing, China

⁸Geological Research Institute of Shandong Gold Group Co., Ltd., Jinan 250013, China

ABSTRACT

The diverse suite of trace elements incorporated into apatite in ore-forming systems has important applications in petrogenesis studies of mineral deposits. Trace element variations in apatite can be used to distinguish between fertile and barren environments, and thus have potential as mineral exploration tools. Such classification approaches commonly employ two-variable scatterplots of apatite trace element compositional data. While such diagrams offer accessible visualization of compositional trends, they often struggle to effectively distinguish ore deposit types because they do not employ all the high-dimensional (i.e., multi-element) information accessible from high-quality apatite trace element analysis. To address this issue, we use a supervised machine-learning-based approach (eXtreme Gradient Boosting, XGBoost) to correlate apatite compositions with ore deposit type, utilizing such high-dimensional information. We evaluated 8629 apatite trace element data from five ore deposit types (porphyry, skarn, orogenic Au, iron oxide copper gold, and iron oxide-apatite) along with unmineralized magmatic and metamorphic apatite to identify discriminating parameters for the individual deposit types, as well as for mineralized systems. According to feature selection, eight elements (Th, U, Sr, Eu, Dy, Y, Nd, and La) improve the model performance. We show that the XGBoost classifier efficiently and accurately classifies high-dimensional apatite trace element data according to the ore deposit type (overall accuracy: 94% and F1 score: 89%). Interpretation of the model using the SHAPley Additive exPlanations (SHAP) tool shows that Th, U, Eu, and Nd are the most indicative elements for classifying deposit types using apatite trace element chemistry. Our approach has broad implications for the better understanding of the sources, chemistry, and evolution of melts and hydrothermal fluids resulting in ore deposit formation.

Keywords: Machine learning, apatite, trace elements, ore deposit fertility, XGBoost, LA-ICP-MS

INTRODUCTION

To develop a quantitative, process-based model for ore-forming systems, a characterization of melt and hydrothermal fluid source, composition and evolution is required (e.g., Andersson et al. 2019). Various minerals in ore-forming systems can constrain the conditions of mineralization based on variations in their mineral chemistry, thus recording the evolution of melts and hydrothermal fluids and yielding constraints on the metallogenic processes (Clark and Williams-Jones 2003; Pisiak et al. 2017; Chapman et al. 2021; Qiu et al. 2021). As a common accessory mineral in igneous, metamorphic, and clastic sedimentary rocks, apatite has a broad range of applications in the geosciences, including thermochronology studies to investigate tectonic

unroofing (Fitzgerald et al. 1991), fault slip rates (Brichau et al. 2006), landscape evolution (Braun et al. 2006), petroleum system maturation (Burtner et al. 1994), and the record of volatile budgets and volcanic eruption triggering (Stock et al. 2016). The structure of apatite also facilitates the substitution of more than half the stable members of the periodic table as trace elements (Hughes 2015), including the rare earth elements and Sr, Y, Th, and U (Sha and Chappell 1999; Chew et al. 2011; Zhou et al. 2022a). Apatite trace element chemistry thus has important applications in igneous and metamorphic petrogenesis studies and in improving the understanding of ore deposit formation (Chu et al. 2009; O'Sullivan et al. 2020; Yu et al. 2021, 2022).

Previous studies that have employed apatite trace element chemistry to classify protolith rock type or fertility have typically employed binary or ternary discrimination diagrams with the variables being apatite trace element abundances or elemental ratios. Belousova et al. (2002) analyzed trace elements in apatite

* E-mail: kunfengqiu@qq.com; djun@cugb.edu.cn

† Orcid 0000-0002-3185-9446

from various common rock types and employed plots of Sr vs. Y and Mn, $(Ce/Yb)_{cn}$ vs. the sum of the REE, and Y vs. Eu/Eu^* to identify fields of apatite compositions from different rock types. Bouzari et al. (2016) used cathodoluminescence combined with trace element compositions to discriminate trace element variations due to alteration linked to the ingress of hydrothermal fluids. Mao et al. (2016) evaluated trace element compositions in apatite from multiple deposit types and suggested several discrimination diagrams for the division of deposit types based on apatite trace element chemistry. O'Sullivan et al. (2020) applied compositional statistics, classification, and a machine learning classifier to apatite trace element compositional data and generated binary plots that discriminated between several types of igneous and metamorphic rocks. Zhou et al. (2022b) used a big data approach to investigate variations in apatite trace element chemistry and showed that an Eu/Y vs. Ce diagram best discriminates apatite crystallized from different host rock types. However, while two-variable scatterplots or three-variable ternary diagrams offer easy and convenient visualization of discrimination trends, they can often fail to rigorously trace the sources, chemistry, and evolution of melts and hydrothermal fluids based on variations in apatite trace element chemistry (Li et al. 2015; Wang et al. 2021; Zhong et al. 2021). The first reason is that apatite has a complex chemistry with high partition coefficients for many trace elements, and trace element partition coefficients in apatite also differ significantly with varying temperature, pressure, and melt compositions (Prowatke and Klemme 2006). The range of possible substitutions in both anion and cation sites and significant tolerance to structural distortion and chemical substitution leads to highly diverse trace element and minor compositions. Another reason is the inherent difficulty of discrimination diagrams resulting in low classification accuracy. Although discrimination diagrams can have a robust geochemical basis, the discrimination fields themselves are defined based on statistics (Pearce 1996). While the geochemical underpinnings of discrimination diagrams may be well understood, they are typically not sufficiently well constrained to accurately predict absolute elemental abundances for chemically complex systems (Snow 2006). In addition, while an individual apatite trace element analysis can yield the abundances of tens of trace elements, discrimination diagrams typically only use the information from two or three variables (element contents and element ratios). Diagnostic geochemical signatures from apatite trace element data may not be effectively extracted from these limited numbers of variables, potentially leading to different types of apatite not being discriminated between or, even worse, misclassified.

High-dimensional analysis methods using machine learning can overcome these challenges. As a rapidly growing approach to analyzing high-throughput experimental data in novel ways, machine learning focuses on the underlying relationships between features (measurable properties) and research targets (Jordan and Mitchell 2015). In recent years, it has been successfully applied to a diverse suite of classification challenges on high-dimensional data sets in the geosciences (Petrelli and Perugini 2016; Schönig et al. 2021; Zhong et al. 2021; Wang et al. 2022). These include estimating pre-eruptive temperatures and pressures using clinopyroxene-melt (Petrelli et al. 2020), evaluating the occurrence of H diffusion in the clinopyroxene

phenocrysts of basaltic magma (Chen et al. 2021), proposing and improving thermobarometry for different magma types [biotite-bearing magma (Li and Zhang 2022); amphibole-bearing magma (Higgins et al. 2022); clinopyroxene-bearing magma (Jorgenson et al. 2022)], and distinguishing S-, I-, and A-type granites (Gion et al. 2022).

In this study, we have compiled a trace element data set comprising 8629 apatite analyses from known mineralization types and ore-barren magmatic rocks from published literature to train and test the classification model. After comparing four commonly employed machine learning algorithms, we chose a scalable end-to-end tree boosting system called XGBoost as the optimal algorithm to tune and yield the final classifiers. XGBoost is an open-source machine-learning algorithm that combines “weak classifiers” to form “strong classifiers” based on a decision tree with gradient boosting (Chen and Guestrin 2016). It provides a rapid and highly accurate approach to classifying high-dimensional data, such as distinguishing between ore-fertile and ore-barren provenance and classifying ore-fertile environments in this study. To address the black box problem commonly attributed to machine learning algorithms resulting from their potential opacity, we employed the SHAPley Additive exPlanations (SHAP) visualization tool (Lundberg and Lee 2017) that makes a machine learning model more explainable by visualizing its output. SHAP is a game theoretic method and applying it reveals the most diagnostic trace elements in apatite for classifying ore deposit types, while also revealing the variable geochemical behavior of different elements in ore deposit types. Our results demonstrate strong correlations between high-dimensional apatite trace-element geochemical data and ore deposit type, thus furthering our knowledge of ore-forming systems, and have broad implications for understanding the sources, chemistry and evolution of melts and hydrothermal fluids.

DATABASE

For the compilation of the apatite trace element data set, 8629 analyses from 1685 rock samples were retrieved from 245 publications using the global petrological open-access database GEOROC (<http://georoc.mpch-mainz.gwdg.de/georoc/>). Apatite trace element compositions from these studies include data from five common ore deposit types located worldwide, including porphyry, skarn, orogenic Au, iron-oxide copper gold (IOCG), and iron-oxide apatite (IOA or Kiruna type) (Fig. 1). Apatite trace element compositions were collected from various unmineralized (barren) magmatic and metamorphic rocks to identify any systematic differences between apatite from fertile and barren systems. Unmineralized samples in the database comprise both wall rocks from the respective mineral deposits but also include non-mineralized regions. As an example, three different types of quartz monzonite porphyry from Jia et al. (2020) were incorporated in our database. Two samples (PD02 and BR04) are ore-fertile samples containing sulfide veins, while sample PD01 is an ore-barren quartz monzonite porphyry containing minimal sulfide. Detailed information on the apatite analyses incorporated in the database is provided in Online Materials¹ Table S1.

Different experimental LA-ICP-MS procedures and protocols employed in the 245 publications result in a diverse suite of trace elements in the compiled data set. The 14 most commonly analyzed

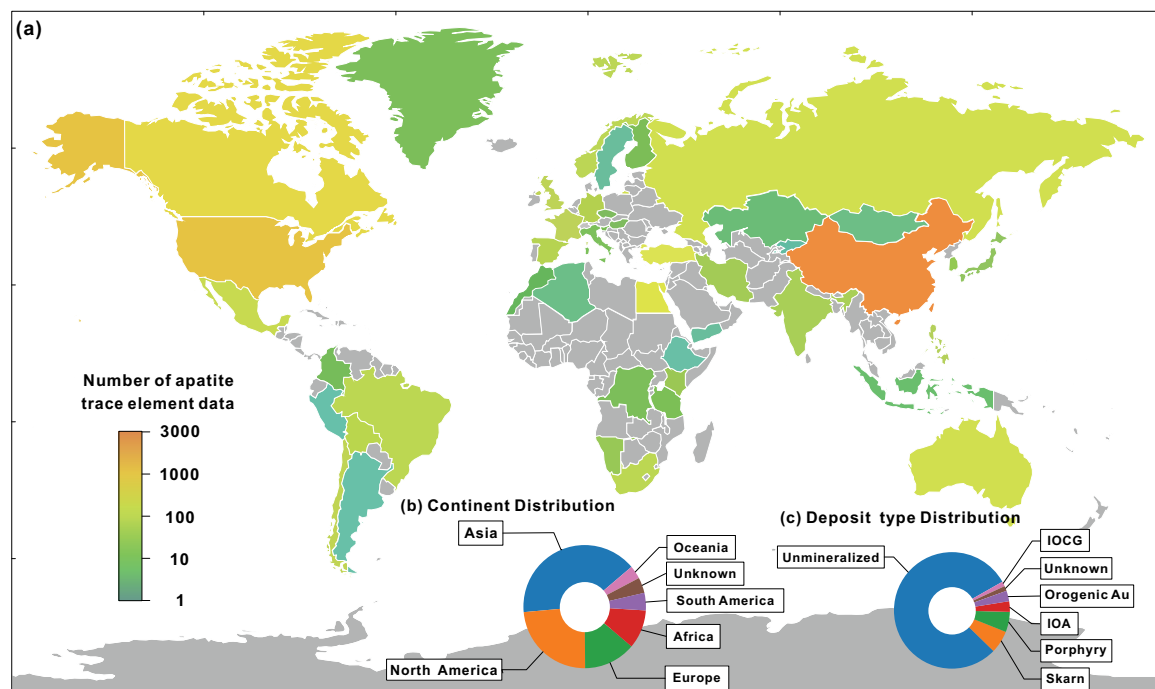


FIGURE 1. Locations of apatite samples investigated in this study. (a) The 245 publications with apatite compositional data cover 49 countries on six continents. Countries are colored according to the number of apatite trace element data (orange high, green low). (b) Pie chart of continent distribution. (c) Pie chart of deposit type distribution. IOCG = iron oxide copper gold deposits; IOA = iron oxide-apatite deposits. (Color online.)

trace elements—La, Ce, Pr, Nd, Sm, Eu, Gd, Dy, Yb, Lu, Sr, Y, Th, and U—were used to provide a consistent and optimized data set. The data set includes values below the detection limit (bdl) or values that were not reported. To improve the quality of the data set, bdl analyses were replaced by a value of half of the detection limit (Zhong et al. 2021). Ultimately the data set was reduced to 4085 analyses from 249 individual samples (unmineralized magmatic apatite: 148; porphyry: 29; skarn: 35; orogenic Au: 15; IOCG: 13; IOA: 9) for further investigation by the different machine learning methods (Table 1). Figure 2 provides a compilation of

the apatite trace element data based on deposit type and individual deposits. Apatite from IOA deposits has the highest La and Th contents, while IOCG apatite has the lowest Sr (Figs. 2a and 2b). These diagrams show that the variation in concentration of some individual elements can distinguish apatite from different types to a certain extent. However, most trace element ranges still overlap and are thus not entirely diagnostic. Therefore, although deposit type is unlikely to be identified using binary or ternary diagrams, the partial separation observed in some of the apatite compositional data implies that machine learning approaches in

TABLE 1. Apatite trace element data description

Deposit type	Apatite type	Location	Country	Selected reference(s)
IOCG	Magmatic/hydrothermal	Wernecke, Bhukia, Wirrda Well prospect, Acropolis prospect	U.S.A., Australia, India	Mao et al. (2016); Mukherjee et al. (2017); Krneta et al. (2017)
IOA	Magmatic/hydrothermal	Durango, Aoshan, Great Bear	Mexico, Canada, China	Mao et al. (2016)
Orogenic Au	Hydrothermal	Congress (Lou), Kirkland Lake, Dentonia, Seabee, Laodou, Xindigou, Hutti	Canada, China, U.S.A., India	Mao et al. (2016); Hazarika et al. (2016); Zhang et al. (2020)
Porphyry	Magmatic/hydrothermal	Boss Mountain, Mount Polley, Shiko, Kemess South, Highmont, Highland Valley, Gibraltar, Brenda, Endako, Cassiar Moly, Dobbin, Lornex, Willa, Daheishan	Canada, China, U.S.A., German, South Africa, Kazakhstan	Cao et al. (2012); Mao et al. (2016); Pan et al. (2016); Xing et al. (2021)
Skarn	Hydrothermal	Racine, Minyari, Little Billie, Gold Canyon, O'Callaghan's, Molly, Yangla, Shuikoushan, Cantung	Canada, China, U.S.A., Kazakhstan	Cao et al. (2012); Mao et al. (2016); Adlakha et al. (2018); Yang et al. (2018); Jia et al. (2020)
Unmineralized	Magmatic	Hawaiian Islands, European orogenic belt, Jan mayen, North Atlantic igneous province, Mexican volcanic belts, Sulawesi Arc	Canada, China, U.S.A., German, South Africa, British, France, Brazil, Chile, Cabo Verde, Russia, Bolivia, Congo, Morocco, Czech, Finland, Greek, Hungary, Italy, Kenya, Norway, Spain, Tanzania, Turkey, Peru	Acosta-Vigil et al. (2010); Laurent et al. (2017); Henrichs et al. (2018); Minissale et al. (2019); Matusiak-Malek et al. (2021); Sun et al. (2021)

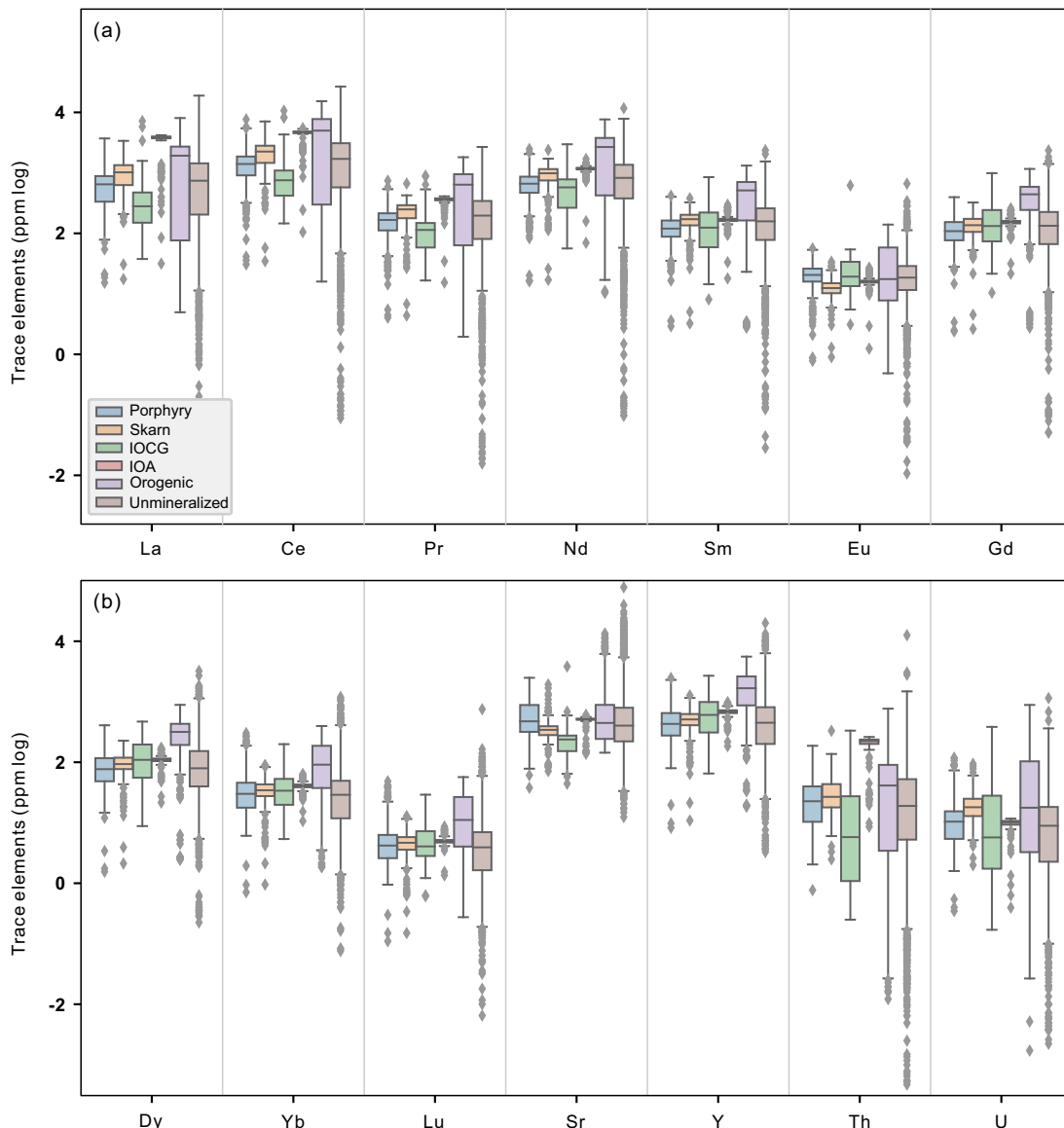


FIGURE 2. Box plots and line plots showing the abundances and dispersion of the selected 14 trace elements in apatite. (a and b) The box plots of data categorized according to deposit types. The height of the colored bars represents the interquartile range (25–75th percentile). The horizontal lines within the colored bars are the median. Whiskers show the 5–95th percentile. The rhombuses (diamond shapes) represent outliers of more than 1.5σ . Unknown denotes the deposit type is known but the locality is not specified. (Color online.)

high-dimensional space have the potential to distinguish apatite derived from different ore deposit types.

Model development and performance

Machine learning is used to teach algorithms to construct self-learning systems which can handle large data sets more efficiently (Jordan and Mitchell 2015; Mahesh 2020). Machine learning is classified into two broad categories: supervised learning and unsupervised learning (Soofi and Awan 2017). In this study, we used supervised machine learning (use of labeled data sets to train algorithms to classify data) to link apatite trace element composition to their source ore-deposit type. We tested four different established algorithms: k-nearest neighbors (KNN)

(Bentley 1975), random forest (RF) (Breiman 2001), support vector machine (SVM) (Vapnik 1995), and eXtreme Gradient Boosting (XGBoost) (Chen et al. 2015), before selecting the best classification model after hyperparameter optimization and comparison. Figure 3 outlines the detailed workflow of our approach.

Data pre-processing

Pre-processing of the data involves standardization and balance processing. A suitable standardization procedure is critical in applying machine learning algorithms, to avoid attributes in greater numeric ranges dominating those in smaller numeric fields, while also helping to eliminate potential numerical difficulties during the calculations in many machine learning approaches (Hsu et al.

2003). We first transformed the data set in this study by applying a log-ratio transformation to obtain a Gaussian distribution, which was then normalized using the “StandardScaler ()” function in the Scikit-learn machine learning library for Python (more detail is provided on the libraries employed in this study). This function centers data by setting the mean to zero for each feature, then scaling it by dividing non-constant features by their standard deviation to produce a standard normal distribution with the mean of observed values = 0 and a standard deviation = 1.

Dealing with imbalanced data are essential prior to building a machine learning model. Many algorithms may be biased toward classes with large sample sizes if the training set is imbalanced. For example, in our data set, 2300 analyses are from unmineralized magmatic apatite, while only 78 analyses are from IOCG deposits. Therefore, we applied the synthetic minority oversampling technique (SMOTE) using the imbalanced-Learn Library in Python to minimize the possible effects resulting from variations in sample size. SMOTE (Chawla et al. 2002) is an improved scheme based on a random oversampling algorithm, which artificially synthesizes new data to add to the data set. Compared with most sampling methods, SMOTE has stronger robustness and achieved the real sense of combining the oversampling minority class and under-sampling majority class.

The selected data set is randomly divided into a training data set (80%) and a testing data set (20%) using the hold-out method while maintaining the exact proportions of each class. The training set was oversampled using the SMOTE algorithm,

which was then used to train the classifier, while the testing set was utilized to evaluate the classifier.

Algorithm comparison

K-nearest neighbors (KNN), random forest (RF), support vector machine (SVM), and eXtreme Gradient Boosting (XGBoost) are widely used machine learning methods that can be applied to the classification of high-dimensional data, and have been commonly used in various fields in the geosciences (Carranza and Laborte 2015; Petrelli et al. 2017; Liu and Beaudoin 2021; Shen et al. 2022). We compared these four supervised machine learning algorithms to select the optimal approach to train the machine learning model for determining ore-deposit type from apatite trace element data.

KNN is one of the simplest classification methods in that it calculates the similarity (proximity) between new and available data. It puts the new data case into the category most similar to the available categories. While this simple classification method has no explicit training step, it is not well suited for large data sets with high dimensionality due to the difficulties in calculating proximities for each data point in high dimensions and does not work well on imbalanced data or data sets with outliers (Bentley 1975; Abu Alfeilat et al. 2019; Nathwani et al. 2022). RF employs an ensemble of decision tree classifiers on various subsamples of the data set and uses averaging to improve the predictive accuracy and control over-fitting (Breiman 2001). RF does not require significant tuning of parameters, tends not to overfit the

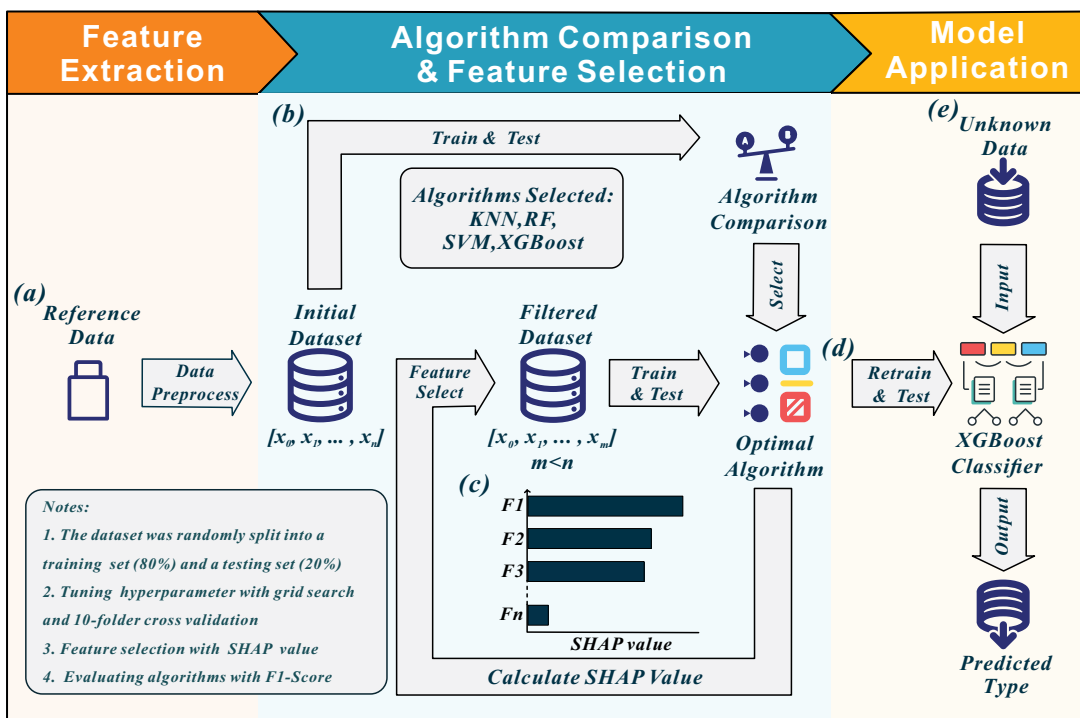


FIGURE 3. Workflow employed to develop the machine learning model. (a) Creating the initial data set after data pre-processing. (b) Using the training data set to train four different algorithms and then using the testing data set to evaluate and compare their performance to select the optimal one. (c) Calculating the SHAP value of each feature (i.e., element) in the initial data set and constructing the filtered data set with the most important (i.e., source-diagnostic) elements. (d) Retraining and testing the chosen algorithm based on the filtered data set to yield the final classifier. (e) Determining the probable deposit type based on the trace element data. (Color online.)

data and can handle nonlinear numeric and categorical predictors. Nevertheless, prediction accuracy on complex problems is generally inferior to that of gradient-boosted trees. RF classification is also more difficult to interpret than a single decision tree (which may be easily visualized as a sequence of decisions and outcomes). The objective of the SVM algorithm is to find a hyperplane in N-dimensional space (where N is the number of features, in this case elements) that distinctly classifies the data points. It is the most commonly used machine learning method in geosciences (Noble 2006; Soofi and Awan 2017), tends not to overfit data nor be overly influenced by outliers, and is most effective in high-dimensional spaces when there is a clear margin of separation between classes. SVM does not perform very well when the data set is noisy (i.e., target classes are overlapping) or on large data sets due to the training time involved. The final SVM model is not probabilistic and can be challenging to interpret and also requires selection of an appropriate kernel function and hyperparameters. XGBoost is a scalable machine learning system that combines “weak classifiers” to form “strong classifiers” based on a decision tree with gradient boosting (Chen and Guestrin 2016). It typically outperforms all other algorithms in machine learning community competitions, can handle large data sets and is not prone to overfitting or the influence of outliers when properly tuned (Nielsen 2016; Abou Omar 2018; Ogunleye and Wang 2020; Wang et al. 2020). It also does not require significant feature processing (i.e., no need for scaling or normalizing data, and it can also handle missing values well); thus feature importance can be ascertained, allowing for feature selection. It does not work well on sparse and unstructured data and can be difficult to tune due to the many hyperparameters involved. Similar to many of the other algorithms described above, interpretation of the final model can be difficult.

Grid search and cross-validation were introduced to optimize hyperparameters as appropriate hyperparameter selection can significantly improve the performance of the machine learning model. Grid search is the traditional approach to hyperparameter optimization, which finds the optimal hyperparameters by conducting a complete search over a given subset of the hyperparameters space of the training algorithm (Liashchynskyi and Liashchynskyi 2019). However, a single grid search is insufficient, and therefore, we used k-fold cross-validation to undertake multiple grid searches using the “GridSearchCV ()” function in Python’s Scikit-learn machine learning library. The training set is divided into k groups, and one subset of data is selected randomly as a validation set and the remainder (k-1) of the subsets as training data sets. This step is repeated for k times to obtain k models, and the average classification accuracy of the final validation set of these k models is used as the performance indicator of the machine learning model.

We performed a grid search with 10-fold cross-validation to tune hyperparameters and used the testing set to evaluate the F1 score (which conveys the balance between the precision and the recall) of the four machine-learning algorithms. We set the random seed while splitting the training and testing sets. This ensures that the data are divided the same way every time the code is run and is also required because algorithms such as RF and XGBoost are non-deterministic (for a given input, the output is not always the same) and thus require a random seed

argument for reproducible results and algorithm comparison. After tuning the hyperparameters, the algorithms yielded the following performance: KNN algorithm (F1 score: 88.6%), random forest algorithm (F1 score: 89.8%), SVM algorithm (F1 score: 89.7%), and XGBoost algorithm (F1 score: 90.8%). Table 2 provides detailed information on the hyperparameters and test scores, and Figure 4 shows the detailed classification information of the four algorithms on a confusion matrix. We chose XGBoost as the optimal supervised machine-learning algorithm as it produced the highest test score and the best and most balanced performance across the five ore deposit categories (Fig. 4).

Feature selection

To effectively apply machine learning methods, feature selection is a key step that helps understand the data, reduces computation and the curse of dimensionality (the explosive nature of increasing data dimensions and its resulting exponential increase in computational efforts), and improves learning performance (Kalousis et al. 2007; Chandrashekar and Sahin 2014; Kumar and Minz 2014; Li et al. 2017). The SHAP tool was employed to compute each trace element’s contribution (SHAP value) in apatite in the initial data set for a particular prediction. We list the SHAP values in descending order in Figure 5 and sequentially added more elements to the XGBoost algorithm in descending SHAP order to show the change (cross-validation and test score) in model performance. As shown in Figure 5, for $n = 1$ (Th), the cross-validation score is ~59%, and the test score was only ~37%. Increasing the number of elements ($n = 5$; Th, U, Sr, Eu, Dy), the cross-validation score increased dramatically to ~98%, with the test score increasing to ~86% ($n = 5$). When $n = 8$, the cross-validation score and test score have stabilized at ~99% and ~90%. The model could hence be built from these eight elements (Th, U, Sr, Eu, Dy, Y, Nd, La) as there is minimal improvement when $n > 8$, which is geologically realistic as the remaining six elements ($n = 9$ to 14) are all REEs which exhibit coupled geochemical behavior. Therefore, to improve the learning performance and the application of the model, we built a filtered data set using the XGBoost method with eight elements (Th, U, Sr, Eu, Dy, Y, Nd, La).

Retraining and testing the classifier

The filtered data set was again randomly split into a training set (80%) and a testing set (20%), and the training set was then oversampled using the SMOTE algorithm and retrained to produce the final XGBoost classifier. Grid search and 10-fold cross-validation were used to choose the optimal hyperparameters (gamma and max_depth, Fig. 6). The classifier was evaluated on the testing set. Randomly splitting the training set and testing set will change the predicted results of the XGBoost model each time, thus, the test

TABLE 2. Optimal hyperparameters and test scores of the four applied algorithms

Algorithms	Best hyperparameters	Hyperparameter cross-validation score	Test score
KNN	n_neighbors = 2; P = 5	99.0%	88.6%
RF	n_estimators = 130	98.8%	89.8%
SVM	C = 64; gamma = 0.5	99.2%	89.7%
XGBoost	n_estimators = 148	98.8%	90.8%

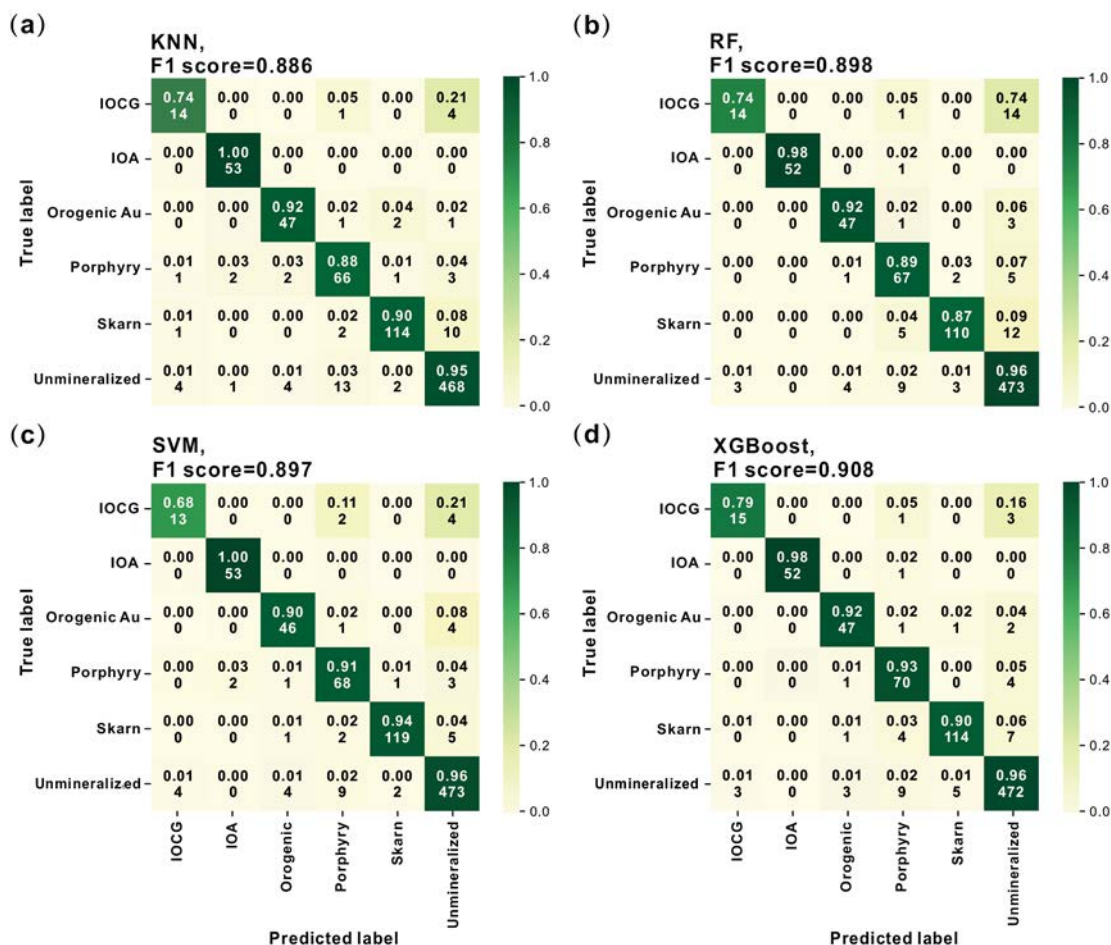


FIGURE 4. Confusion matrix of the testing set used to evaluate the accuracy of the four algorithms. (a) KNN. (b) Random forest. (c) SVM. (d) XGBoost. The algorithm method and its respective F1 score are presented above each panel while the numbers at the top and bottom of each square represent the proportion of predicted deposit types and the number of predicted deposit types, respectively. (Color online.)

scores (mean score ± standard deviation) were calculated from 50 iterations. The optimal XGBoost classification was determined for hyperparameters of *n_estimators* = 148, *gamma* = 0, *max_depth* = 9. (Table 3), with a precision of 0.89 ± 0.02, recall of 0.90 ± 0.02, F1 score of 0.89 ± 0.02, and accuracy of 0.94 ± 0.01. Figure 6 shows the F1 score of different hyperparameter combinations. A summary of the precision, recall, and F1 score for each class is provided in Table 3.

Libraries

All operations on the reference data set from pre-processing through to model application were undertaken using the Python programming language. The following libraries were used to complete the code: pandas (Snider and Swedo 2004), numpy (Oliphant 2006), and imlearn (Ma and He 2013) for data analysis; matplotlib (Barrett et al. 2005) and seaborn (Waskom 2021) for plotting the diagrams; scikit-learning (Kramer 2016) and xgboost (Chen et al. 2015) for machine learning; and shap (Lundberg and Lee 2017) for feature selection and machine learning interpretation.

DISCUSSION

Limitations of 2D classification diagrams employing two variables

The potential limitations of employing discrimination diagrams (e.g., 2D scatterplots with two variables) were initially discussed in the introduction and are explored further here. In this study, we first calculated the ratio of two random elements from the data set and added them into the data set as new features. A total of 5460 discrimination diagrams were constructed using any two features in the data set with the best discrimination combination represented by a plot of Th/Pr vs. U/Pr ratio (Fig. 7a), with the silhouette coefficient used to investigate the separation distance between the resulting clusters. We also investigated the six elements (Th, U, Sr, Eu, Dy, and Y) with the highest SHAP values (Fig. 5) to draw 2D scatterplots (Figs. 7b, 7c, and 7d).

As shown in Figure 7, these four discrimination diagrams cannot effectively distinguish between an ore-fertile and ore-barren provenance. Apatite data from different ore-fertile environments overlap as well. This is the principal limitation of two-variable scatterplots—they only employ a small amount of information

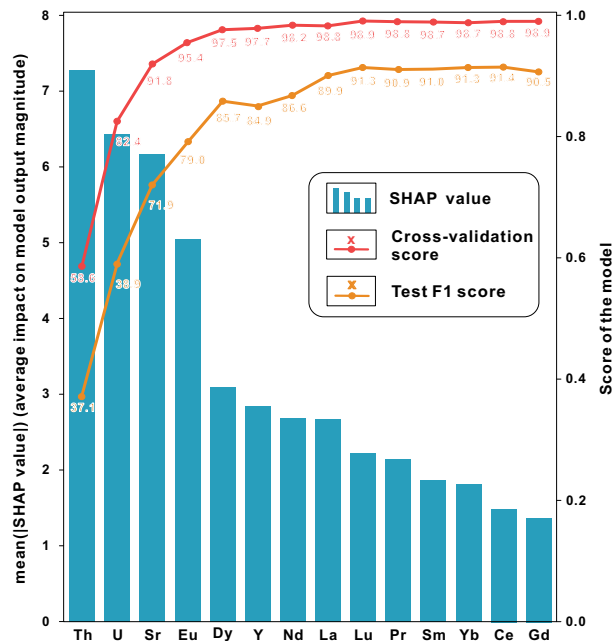


FIGURE 5. The mean SHAP value of each element and test F1 and cross-validation scores of the XGBoost model. The bar plot shows the mean SHAP value of each element, which reflects its contribution to the model prediction. The lines reflect the change in algorithm performance with increasing number of elements (red = cross-validation score; orange = test F1 score). (Color online.)

TABLE 3. Evaluation of 50 iterations of the final XGBoost classifier

	Precision	Recall	F1 score	Support
IOCG	0.70 ± 0.12	0.74 ± 0.12	0.71 ± 0.09	15.80 ± 3.63
IOA	0.99 ± 0.01	0.98 ± 0.02	0.98 ± 0.01	52.08 ± 5.26
Orogenic Au	0.91 ± 0.03	0.90 ± 0.04	0.90 ± 0.03	49.33 ± 6.40
Porphyry	0.86 ± 0.04	0.87 ± 0.04	0.87 ± 0.03	84.57 ± 7.71
Skarn	0.93 ± 0.03	0.92 ± 0.03	0.92 ± 0.02	108.61 ± 11.11
Unmineralized	0.96 ± 0.01	0.96 ± 0.01	0.96 ± 0.01	506.61 ± 13.78
Accuracy			0.94 ± 0.01	817.00
Macro avg.	0.89 ± 0.02	0.90 ± 0.02	0.89 ± 0.02	817.00
Weighted avg.	0.94 ± 0.01	0.94 ± 0.01	0.94 ± 0.01	817.00

from the high-dimensional data, unlike the high-dimensional machine learning approach undertaken in this study. Even though the apatite trace element data from the different ore deposit types overlap, the apatite data from individual deposit types still cluster together on the four discrimination diagrams (Fig. 7). Unsurprisingly given the extremely broad variation in apatite trace element abundances in igneous rocks (O’Sullivan et al. 2020), the unmineralized magmatic apatite field is by far the largest, encompassing nearly all the ore deposit fields. The unmineralized magmatic apatite field exhibits bimodal Sr (Fig. 7b) and U abundances (Fig. 7c). This corroborates the findings of O’Sullivan et al. (2020), with U abundances low in ultramafic igneous and low-grade metamorphic apatite and higher in igneous and high-grade metamorphic apatite, and Sr low in all metamorphic rocks and I- and S-type igneous rocks, and higher in alkaline and ultramafic igneous rocks (Fig. 6 in O’Sullivan et al. 2020).

Apatite from IOA deposits define relatively restricted fields on all discrimination plots (Fig. 7), while those from orogenic

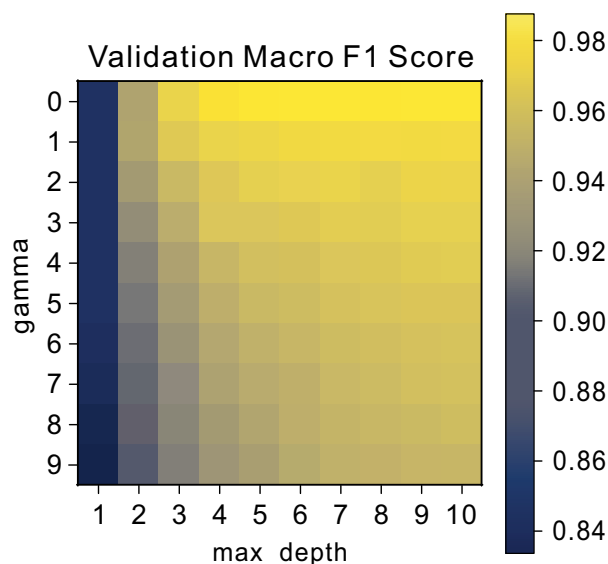


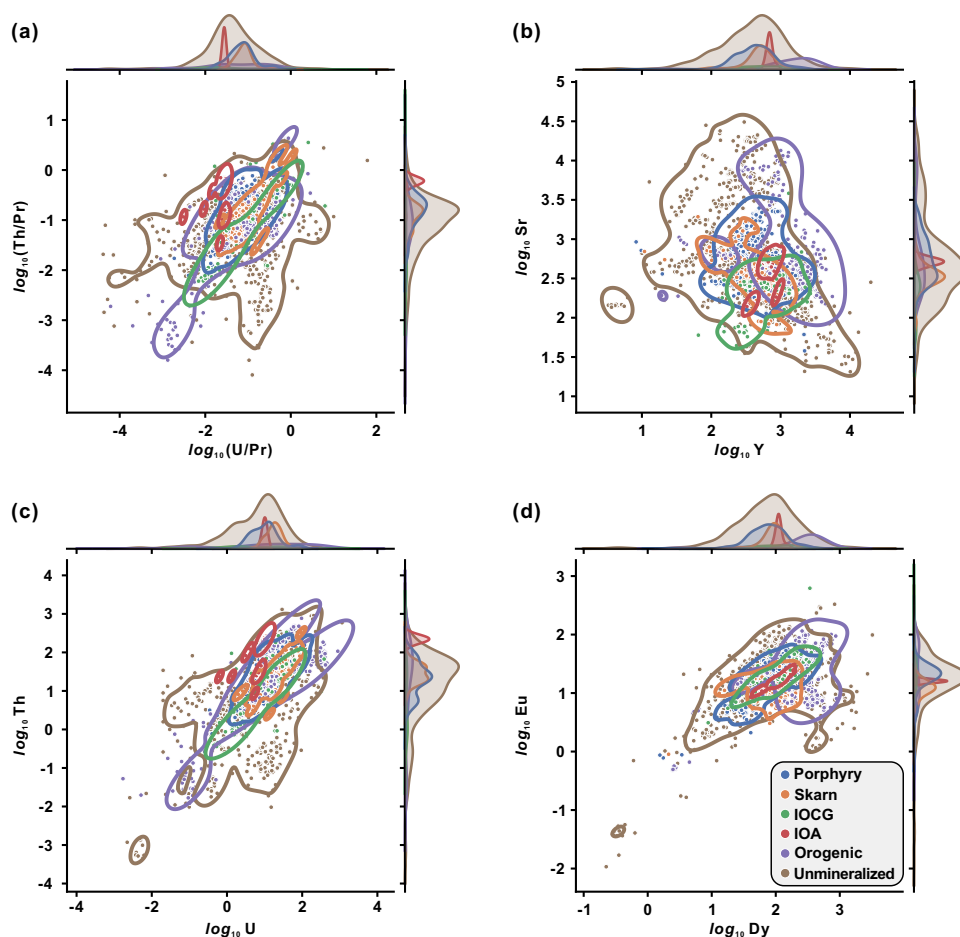
FIGURE 6. The cross-validation F1-score across the gamma and max_depth grid search. The optimal combination is gamma = 0 and max_depth = 9. (Color online.)

Au deposits show higher concentrations of Y and the geochemically similar element Dy (Figs. 7b and 7d). The kernel density curves of Sr contents in apatite from orogenic Au deposits also have two distinct peaks (Fig. 7b). The kernel density curves of Eu and U abundances show that apatite from skarn deposits have lower concentrations of Eu and higher abundances of U compared with apatite from porphyry deposits (Figs. 7c and 7d). These observations show that the trace element abundances of apatite from different ore deposits exhibit systematic trace element variations and thus have the potential to be discriminated effectively using the high-dimensional data space through the machine learning approach adopted in this study.

Classification in high-dimensional space

The classifier can effectively distinguish between ore-fertile and ore-barren environments (recall ratio >95% for barren samples), and apatite from the different deposit types can also be successfully distinguished with F1 test scores of >88% for all four algorithms (Fig. 4). This suggests that classifying deposit types using machine learning applied to apatite compositional data are a viable approach. The exception is IOCG apatite, for which 16% of analyses were predicted to belong to different classes (Fig. 8), probably due to the small sample amount of this deposit type, even though SMOTE oversampled the training set. The predictions for porphyry and skarn deposits are better. However, both are less than 90% (porphyry deposits: 89%, skarn deposits: 88%), which is attributed mainly to the complexity of porphyry and skarn mineralization processes. Porphyry mineralization takes place across a very broad temperature range from 250 to 1000 °C, and apatite forming during different porphyry crystallization stages may have very different trace element signatures (Sillitoe 2010). Skarn mineralization also occurs across a wide range of formation temperatures, while the diverse nature of host rock types in skarn systems may impart additional trace element

FIGURE 7. Scatterplots and kernel density curves for different apatite trace element or element ratio combinations. (a) Th/Pr vs. U/Pr. (b) Sr vs. Y. (c) Th vs. U. (d) Eu vs. Dy. (Color online.)



variability (Jia et al. 2020). Future work could include a subdivision of apatite classes to incorporate differing crystallization stages and host rock chemistries in porphyry and skarn systems, although this is likely to be a substantial undertaking. Nevertheless, the XGBoost classifier performs well on the classification of fertility and all deposit types in this data set with an overall accuracy >94% and F1 score >89%, with both high precision and recall ratios, especially for the IOA and orogenic Au deposits, from which almost all apatite data are predicted correctly (Fig. 8).

Low-grade metamorphic apatite is very similar in terms of its trace element geochemistry to hydrothermal apatite (O’Sullivan et al. 2020). Therefore, an effective machine learning model must distinguish low-grade metamorphic apatite

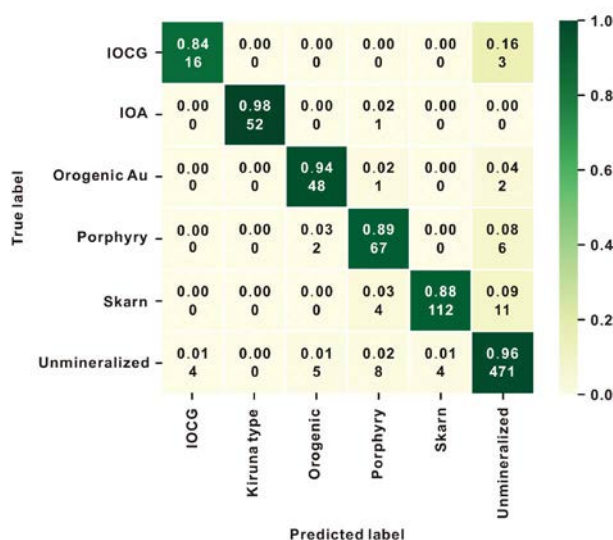


FIGURE 8. Confusion matrix of the testing set to evaluate the accuracy of the XGBoost classifier. The numbers in the top and bottom of each square represent the proportion of predicted deposit types and the number of predicted deposit types, respectively. Note the score in this confusion matrix and the evaluation report (Table 3) differ slightly from the scores presented in the confusion matrix in Figure 4. In this figure and Table 3, the XGBoost model was optimized further to use three hyperparameters (*n_estimators*, *gamma*, and *max_depth*) and the splitting of the training set and testing set was iterated 50 times, both of which improved the classifier accuracy. (Color online.)

from the five mineralized classes. We selected 215 apatite analyses from 31 samples from the database of O’Sullivan et al. (2020) with different metamorphic grades (high-grade metamorphic apatite: 112; low- and medium-grade metamorphic

apatite: 103) as a new testing set. Based on the XGBoost classifier, our predicted results show that most of the analyses accurately classified unmineralized apatite (181 out of 215, Online Materials¹ Table S2). Fourteen high-grade metamorphic apatite analyses were misclassified as IOCG apatite, while 98 high-grade metamorphic apatite analyses were correctly predicted as unmineralized apatite. For low- and medium-grade metamorphic apatite, 20 apatites were misclassified as a mineralized class (15 apatites predicted as orogenic Au, three apatites predicted as porphyry, one apatite predicted as skarn and one apatite predicted as IOA). In contrast, the remaining 83 apatites were predicted correctly. The performance (overall accuracy >84%) on this group of metamorphic samples shows that our XGBoost classifier can effectively distinguish low-grade metamorphic apatite from fertile classes and provides a rapid and highly accurate approach to predicting ore deposit type based on apatite trace element data.

Interpreting machine learning models

Machine learning methods have been widely used in geosciences and various algorithms have been proven to be useful tools for interpreting high-dimensional geochemical data (Petrelli and Perugini 2016; Chen et al. 2021; Wang et al. 2021). Despite their widespread application in the classification of big data sets, machine learning approaches are often referred to as a black box, where the data set undergoes a series of calculations immediately followed by the output of results, without providing a transparent working process between the input and output data (Lancet Respiratory Medicine 2018). Some studies have employed feature importance to select machine learning training parameters (Nathwani et al. 2022). However, such an approach does not help show the relationship between a given feature and the working target—feature importance is based on the decrease in model performance and contains no information beyond this. To improve the transparency and interpretation of our XGBoost classifier, a SHAP summary plot is presented in Figure 9. This summary plot combines feature importance with the magnitude of feature attributes, and features are ordered according to their importance. Each point on the summary plot is a SHAP value for a feature and an instance. The feature importance determines the position on the y-axis and on the x-axis by the SHAP value, while the color represents the value of the feature from low to high.

Sr and Eu are the two most diagnostic elements for classifying IOCG deposits. For example, high concentrations of Sr (red colors) negatively influence the classification while low concentrations have a positive influence; the relationship is the opposite for Eu (Fig. 9a). For IOA deposits, high-Th contents, low-U abundances and low Sr favor prediction as an IOA deposit (Fig. 9b). Porphyry deposit apatite classification is favored by low Th and low Nd (Fig. 9c) while low-U and -Eu abundances help to distinguish skarn deposits. The lowest U concentrations may be partly affected by values below the limit of detection. A larger data set should confirm the relationship between apatite U contents and skarn deposits (Fig. 9d). High concentrations of Dy and Sr help classify orogenic Au deposits (Fig. 9e). Although there is wide variation in apatite trace element abundances in different types of igneous and metamorphic rocks (O'Sullivan

et al. 2020) and the unmineralized magmatic apatite data set is very large and diverse, moderate Th and, in particular, high Nd are indicative for unmineralized apatite (Fig. 9f).

In summary, Th, U, Eu, and Nd are the most effective elements for classifying ore deposit types, especially Th for IOA (Fig. 9b), Nd for porphyry and unmineralized apatite (Figs. 9c and 9f), U for skarn (Fig. 9d), and Dy for orogenic Au deposits (Fig. 9e). Other elements, like Sr, also improves the classification of some deposit types (Figs. 9a and 9e).

IMPLICATIONS

Traditional methods to discriminate (e.g., using two-variable scatterplots) only result in partial separation of ore deposit classes because of the complexity of apatite chemistry. The machine learning-based approach (XGBoost) fully exploits the high dimensionality of apatite trace element data to produce a novel geochemical classification system to link apatite trace element chemistry with ore deposit type. With the increasing amounts of high-throughput apatite trace element data produced by modern analytical techniques, our XGBoost approach offers the potential to make more data-driven decisions, such as subdivision of porphyry and skarn mineralization stages. Moreover, the novel SHAP-based analysis approach aids understanding of the sources, chemistry, and evolution of mineralizing melts and fluids in ore deposit studies.

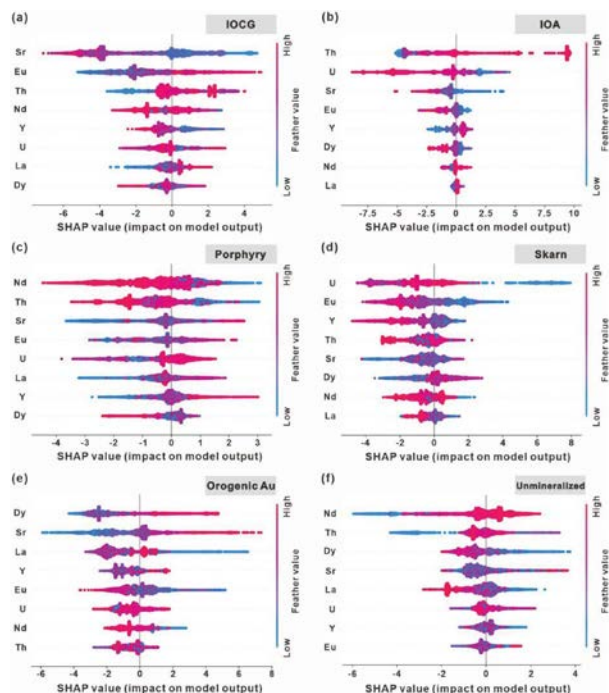


FIGURE 9. SHAP summary plots of apatite trace element data various deposit types. (a) IOCG. (b) IOA. (c) Porphyry. (d) Skarn. (e) Orogenic Au. (f) Unmineralized rocks. Each line represents one element from the data set in decreasing order of importance, and the abscissa is the SHAP value. When the SHAP value exceeds 0, the feature has a positive impact and vice versa. A small circle (dot) represents an individual analysis and the color represents the concentration of the respective element (red = high, blue = low). (Color online.)

DATA AVAILABILITY STATEMENT

The data set and code are available on the Zenodo website (<https://doi.org/10.5281/zenodo.7094836>).

ACKNOWLEDGMENTS

We gratefully acknowledge the constructive comments of Don Baker, Associate Editor Maurizio Petrelli, Oliver Higgins, and anonymous journal reviewers.

FUNDING

This work was financially supported by the National Key Research Program (2023YFE0125000 and 2023YFF0804200), the National Natural Science Foundation of China (42261134535 and 42072087), the Frontiers Science Center for Deep-time Digital Earth (2652023001), and the 111 Project (BP0719021). David Chew acknowledges past and present support from Science Foundation Ireland (SFI) under Grant Numbers 12/IP/1663 and 13/RC/2092_P2 (iCRAG, the SFI Research Centre in Applied Geosciences).

REFERENCES CITED

Abou Omar, K.B. (2018) XGBoost and LGBM for Porto Seguro’s Kaggle challenge: A comparison. ETH Preprint Semester Project, <https://pub.tik.ee.ethz.ch/students/2017-HS/SA-2017-98.pdf>.

Abu Alfeilat, H.A., Hassanat, A.B.A., Lasassmeh, O., Tarawneh, A.S., Alhasanat, M.B., Eyal Salman, H.S., and Prasath, V.B.S. (2019) Effects of distance measure choice on K-nearest neighbor classifier performance: A review. *Big Data*, 7, 221–248, <https://doi.org/10.1089/big.2018.0175>.

Acosta-Vigil, A., Buick, I., Hermann, J., Cesare, B., Rubatto, D., London, D., and Morgan, G.B. (2010) Mechanisms of crustal anatexis: A geochemical study of partially melted metapelite enclaves and host dacite, SE Spain. *Journal of Petrology*, 51, 785–821, <https://doi.org/10.1093/petrology/egp095>.

Adlakha, E., Hanley, J., Falck, H., and Boucher, B. (2018) The origin of mineralizing hydrothermal fluids recorded in apatite chemistry at the Cantung W-Cu skarn deposit, NWT, Canada. *European Journal of Mineralogy*, 30, 1095–1113, <https://doi.org/10.1127/ejm/2018/0030-2780>.

Andersson, S.S., Wagner, T., Jonsson, E., Fusswinkel, T., and Whitehouse, M.J. (2019) Apatite as a tracer of the source, chemistry and evolution of ore-forming fluids: The case of the Olsorum-Djupedal REE-phosphate mineralisation, SE Sweden. *Geochimica et Cosmochimica Acta*, 255, 163–187, <https://doi.org/10.1016/j.gca.2019.04.014>.

Barrett, P., Hunter, J., Miller, J.T., Hsu, J.C., and Greenfield, P. (2005) matplotlib—A Portable Python Plotting Package. *Astronomical Data Analysis Software and Systems XIV ASP Conference*, 347, 91.

Belousova, E.A., Griffin, W.L., O’Reilly, S.Y., and Fisher, N.I. (2002) Apatite as an indicator mineral for mineral exploration: Trace-element compositions and their relationship to host rock type. *Journal of Geochemical Exploration*, 76, 45–69, [https://doi.org/10.1016/S0375-6742\(02\)00204-2](https://doi.org/10.1016/S0375-6742(02)00204-2).

Bentley, J.L. (1975) Multidimensional binary search trees used for associative searching. *Communications of the ACM*, 18, 509–517, <https://doi.org/10.1145/361002.361007>.

Bouzari, F., Hart, C.J., Bissig, T., and Barker, S. (2016) Hydrothermal alteration revealed by apatite luminescence and chemistry: A potential indicator mineral for exploring covered porphyry copper deposits. *Economic Geology and the Bulletin of the Society of Economic Geologists*, 111, 1397–1410, <https://doi.org/10.2113/econgeo.111.6.1397>.

Braun, J., van der Beek, P., and Batt, G. (2006) *Quantitative Thermochronology: Numerical Methods for the Interpretation of Thermochronological Data*, 272 p. Cambridge University Press.

Breiman, L. (2001) Random forests. *Machine Learning*, 45, 5–32.

Brichau, S., Ring, U., Ketcham, R.A., Carter, A., Stockli, D., and Brunel, M. (2006) Constraining the long-term evolution of the slip rate for a major extensional fault system in the central Aegean, Greece, using thermochronology. *Earth and Planetary Science Letters*, 241, 293–306, <https://doi.org/10.1016/j.epsl.2005.09.065>.

Burtner, R.L., Nigrini, A., and Donehick, R.A. (1994) Thermochronology of Lower Cretaceous source rocks in the Idaho-Wyoming thrust belt. *AAPG Bulletin*, 78, 1613–1636.

Cao, M., Li, G., Qin, K., Seitmuratova, E.Y., and Liu, Y. (2012) Major and trace element characteristics of apatites in granitoids from Central Kazakhstan: Implications for petrogenesis and mineralization. *Resource Geology*, 62, 63–83, <https://doi.org/10.1111/j.1751-3928.2011.00180.x>.

Carranza, E.J.M. and Laborte, A.G. (2015) Random forest predictive modeling of mineral prospectivity with small number of prospects and data with missing values in Abra (Philippines). *Computers & Geosciences*, 74, 60–70, <https://doi.org/10.1016/j.cageo.2014.10.004>.

Chandrashekar, G. and Sahin, F. (2014) A survey on feature selection methods. *Computers & Electrical Engineering*, 40, 16–28, <https://doi.org/10.1016/j.compeleceng.2013.11.024>.

Chapman, R.J., Moles, N.R., Bluemel, B., and Walshaw, R.D. (2021) Detrital gold as an indicator mineral. *Geological Society of London, Special Publications*, 516, 313–336.

Chawla, N.V., Bowyer, K.W., Hall, L.O., and Kegelmeyer, W.P. (2002) SMOTE: Synthetic minority over-sampling technique. *Journal of Artificial Intelligence Research*, 16, 321–357, <https://doi.org/10.1613/jair.953>.

Chen, T. and Guestrin, C. (2016) Xgboost: A scalable tree boosting system. *Proceedings of the 22nd ACM SIGKDD International Conference on Knowledge Discovery and Data Mining*, p. 785–794, <https://doi.org/10.1145/2939672.2939785>.

Chen, T., He, T., Benesty, M., Khotilovich, V., Tang, Y., Cho, H., and Chen, K. (2015) Xgboost: Extreme gradient boosting. *R Package Version 0.4–2*, 1, 1–4.

Chen, H., Su, C., Tang, Y.Q., Li, A.Z., Wu, S.S., Xia, Q.K., and Zhang Zhou, J. (2021) Machine learning for identification of primary water concentrations in mantle pyroxene. *Geophysical Research Letters*, 48, e2021GL095191.

Chew, D.M., Sylvester, P.J., and Tubrett, M.N. (2011) U-Pb and Th-Pb dating of apatite by LA-ICPMS. *Chemical Geology*, 280, 200–216, <https://doi.org/10.1016/j.chemgeo.2010.11.010>.

Chu, M.F., Wang, K.L., Griffin, W.L., Chung, S.L., O’Reilly, S.Y., Pearson, N.J., and Iizuka, Y. (2009) Apatite composition: Tracing petrogenetic processes in Transhimalayan granitoids. *Journal of Petrology*, 50, 1829–1855, <https://doi.org/10.1093/petrology/egp054>.

Clark, J.R., and Williams-Jones, A.E. (2003) Rutile as a potential indicator mineral for metamorphosed metallic ore deposits. *Rapport Final de DIVEX, Sous-projet SC2*, 17.

Fitzgerald, P., Fryxell, J., and Wemick, B. (1991) Miocene crustal extension and uplift in southeastern Nevada: Constraints from fission track analysis. *Geology*, 19, 1013–1016, [https://doi.org/10.1130/0091-7613\(1991\)019<1013:MCEAU>2.CO;2](https://doi.org/10.1130/0091-7613(1991)019<1013:MCEAU>2.CO;2).

Gion, A.M., Piccoli, P.M., and Candela, P.A. (2022) Characterization of biotite and amphibole compositions in granites. *Contributions to Mineralogy and Petrology*, 177, 43, <https://doi.org/10.1007/s00410-022-01908-7>.

Hazarika, P., Mishra, B., and Pruseth, K.L. (2016) Scheelite, apatite, calcite and tourmaline compositions from the late Archean Huttu orogenic gold deposit: Implications for analogous two stage ore fluids. *Ore Geology Reviews*, 72, 989–1003, <https://doi.org/10.1016/j.oregeorev.2015.09.004>.

Henrichs, I.A., O’Sullivan, O., Chew, D.M., Mark, C., Babechuk, M.G., McKenna, C., and Emo, R. (2018) The trace element and U-Pb systematics of metamorphic apatite. *Chemical Geology*, 483, 218–238, <https://doi.org/10.1016/j.chemgeo.2017.12.031>.

Higgins, O., Sheldrake, T., and Caricchi, L. (2022) Machine learning thermobarometry and chemometry using amphibole and clinopyroxene: A window into the roots of an arc volcano (Mount Liamuiga, Saint Kitts). *Contributions to Mineralogy and Petrology*, 177, 1–22.

Hsu, C.W., Chang, C.C., and Lin, C.J. (2003) A practical guide to support vector classification. Department of Computer Science, National Taiwan University, <https://www.csie.ntu.edu.tw/~cjlin/papers/guide/guide.pdf>.

Hughes, J.M. (2015) The many facets of apatite. *American Mineralogist*, 100, 1033–1039.

Jia, F., Zhang, C., Liu, H., Meng, X., and Kong, Z. (2020) In situ major and trace element compositions of apatite from the Yangla skarn Cu deposit, southwest China: Implications for petrogenesis and mineralization. *Ore Geology Reviews*, 127, 103360, <https://doi.org/10.1016/j.oregeorev.2020.103360>.

Jordan, M.I. and Mitchell, T.M. (2015) Machine learning: Trends, perspectives, and prospects. *Science*, 349, 255–260, <https://doi.org/10.1126/science.aaa8415>.

Jorgenson, C., Higgins, O., Petrelli, M., Bégue, F., and Caricchi, L. (2022) A machine learning-based approach to clinopyroxene thermobarometry: Model optimization and distribution for use in earth sciences. *Journal of Geophysical Research: Solid Earth*, 127, e2021JB022904, <https://doi.org/10.1029/2021JB022904>.

Kalousis, A., Prados, J., and Hilario, M. (2007) Stability of feature selection algorithms: A study on high-dimensional spaces. *Knowledge and Information Systems*, 12, 95–116, <https://doi.org/10.1007/s10115-006-0040-8>.

Kramer, O. (2016) Scikit-learn. In *Machine Learning for Evolution Strategies*, 45–53. Springer.

Krneta, S., Cook, N.J., Ciobanu, C.L., Ehrig, K., and Kontonikas-Charos, A. (2017) The Wirra Well and Acropolis prospects, Gawler Craton, South Australia: Insights into evolving fluid conditions through apatite chemistry. *Journal of Geochemical Exploration*, 181, 276–291, <https://doi.org/10.1016/j.gexplo.2017.08.004>.

Kumar, V. and Minz, S. (2014) Feature selection: A literature review. *SmartCR*, 4, 211–229, <https://doi.org/10.6029/smartcr.2014.03.007>.

Lancet Respiratory Medicine (2018) Opening the black box of machine learning. *Lancet Respiratory Medicine*, 6, 801.

Laurent, O., Zeh, A., Gerdes, A., Villaros, A., Gros, K., and Slaby, E. (2017) How do granitoid magmas mix with each other? Insights from textures, trace element and Sr-Nd isotopic composition of apatite and titanite from the Matok pluton (South Africa). *Contributions to Mineralogy and Petrology*, 172, 80, <https://doi.org/10.1007/s00410-017-1398-1>.

Li, X. and Zhang, C. (2022) Machine learning thermobarometry for biotite-bearing magmas. *Journal of Geophysical Research: Solid Earth*, 127, e2022JB024137.

Li, C., Arndt, N.T., Tang, Q., and Ripley, E.M. (2015) Trace element indiscrimination diagrams. *Lithos*, 232, 76–83, <https://doi.org/10.1016/j.lithos.2015.06.022>.

Li, J., Cheng, K., Wang, S., Morstatter, F., Trevino, R.P., Tang, J., and Liu, H. (2017) Feature selection: A data perspective. *ACM Computing Surveys*, 50, 1–45.

Liashchynskiy, P. and Liashchynskiy, P. (2019) Grid search, random search, genetic algorithm: A big comparison for NAS. *arXiv preprint*, <https://doi.org/10.48550/arXiv.1912.06059>.

- Liu, H. and Beaudoin, G. (2021) Geochemical signatures in native gold derived from Au-bearing ore deposits. *Ore Geology Reviews*, 132, 104066, <https://doi.org/10.1016/j.oregeorev.2021.104066>.
- Lundberg, S.M. and Lee, S.I. (2017) A unified approach to interpreting model predictions. *Advances in Neural Information Processing Systems* 30. NIPS'17: Proceedings of the 31st International Conference on Neural Information Processing Systems December 2017, 4768–4777, <https://doi.org/10.48550/arXiv.1705.07874>.
- Ma, Y. and He, H., Eds. (2013) *Imbalanced Learning: Foundations, Algorithms, and Applications*, 216 p. Wiley-IEEE Press.
- Mahesh, B. (2020) Machine learning algorithms—a review. *International Journal of Science and Research*, 9, 381–386.
- Mao, M., Rukhlov, A.S., Rowins, S.M., Spence, J., and Coogan, L.A. (2016) Apatite trace element compositions: A robust new tool for mineral exploration. *Economic Geology and the Bulletin of the Society of Economic Geologists*, 111, 1187–1222, <https://doi.org/10.2113/econgeo.111.5.1187>.
- Matusiak-Malek, M., Puziewicz, J., Ntafos, T., Woodland, A., Uenver-Thiele, L., Büchner, J., Grégoire, M., and Aulbach, S. (2021) Variable origin of clinopyroxene megacrysts carried by Cenozoic volcanic rocks from the eastern limb of Central European Volcanic Province (SE Germany and SW Poland). *Lithos*, 382–383, 105936, <https://doi.org/10.1016/j.lithos.2020.105936>.
- Minissale, S., Zanetti, A., Tedesco, D., Morra, V., and Melluso, L. (2019) The petrology and geochemistry of Nyiragongo lavas of 2002, 2016, 1977 and 2017 AD, and the trace element partitioning between melilitite glass and melilite, nepheline, leucite, clinopyroxene, apatite, olivine and Fe-Ti oxides: A unique scenario. *Lithos*, 332–333, 296–311, <https://doi.org/10.1016/j.lithos.2019.02.023>.
- Mukherjee, R., Venkatesh, A.S., and Fareeduddin. (2017) Chemistry of magnetite-apatite from albite and carbonate-hosted Bhukia Gold Deposit, Rajasthan, western India—An IOCG-IOA analogue from Paleoproterozoic Aravalli Supergroup: Evidence from petrographic, LA-ICP-MS and EPMA studies. *Ore Geology Reviews*, 91, 509–529, <https://doi.org/10.1016/j.oregeorev.2017.09.005>.
- Nathwani, C.L., Wilkinson, J.J., Fry, G., Armstrong, R.N., Smith, D.J., and Ihlenfeld, C. (2022) Machine learning for geochemical exploration: Classifying metallogenetic fertility in arc magmas and insights into porphyry copper deposit formation. *Mineralium Deposita*, 57, 1143–1166, <https://doi.org/10.1007/s00126-021-01086-9>.
- Nielsen, D. (2016) Tree boosting with xgboost—why does XGBoost win “every” machine learning competition? Master’s thesis, NTNU.
- Noble, W.S. (2006) What is a support vector machine? *Nature Biotechnology*, 24, 1565–1567, <https://doi.org/10.1038/nbt1206-1565>.
- Ogunleye, A. and Wang, Q.G. (2020) XGBoost model for chronic kidney disease diagnosis. *IEEE/ACM Transactions on Computational Biology and Bioinformatics*, 17, 2131–2140, <https://doi.org/10.1109/TCBB.2019.2911071>.
- Oliphant, T.E. (2006) *A guide to NumPy*. Volume 1, 85. Trelgol Publishing.
- O’Sullivan, G., Chew, D., Kenny, G., Henrichs, I., and Mulligan, D. (2020) The trace element composition of apatite and its application to detrital provenance studies. *Earth-Science Reviews*, 201, 103044, <https://doi.org/10.1016/j.earscirev.2019.103044>.
- Pan, L.C., Hu, R.Z., Wang, X.S., Bi, X.W., Zhu, J.J., and Li, C. (2016) Apatite trace element and halogen compositions as petrogenetic-metallogenetic indicators: Examples from four granite plutons in the Sanjiang region, SW China. *Lithos*, 254–255, 118–130, <https://doi.org/10.1016/j.lithos.2016.03.010>.
- Pearce, J.A. (1996) A user’s guide to basalt discrimination diagrams. In D.A. Wyman, Ed., *Trace Element Geochemistry of Volcanic Rocks: Applications for massive sulphide exploration*. Geological Association of Canada, Short Course Notes, 12, 79–113.
- Petrelli, M. and Perugini, D. (2016) Solving petrological problems through machine learning: The study case of tectonic discrimination using geochemical and isotopic data. *Contributions to Mineralogy and Petrology*, 171, 81, <https://doi.org/10.1007/s00410-016-1292-2>.
- Petrelli, M., Bizzarri, R., Morgavi, D., Balzanza, A., and Perugini, D. (2017) Combining machine learning techniques, microanalyses and large geochemical datasets for tephrochronological studies in complex volcanic areas: New age constraints for the Pleistocene magmatism of central Italy. *Quaternary Geochronology*, 40, 33–44, <https://doi.org/10.1016/j.quageo.2016.12.003>.
- Petrelli, M., Caricchi, L., and Perugini, D. (2020) Machine learning thermo-barometry: Application to clinopyroxene-bearing magmas. *Journal of Geophysical Research: Solid Earth*, 125, e2020JB020130.
- Pisiak, L.K., Canil, D., Lacourse, T., Plouffe, A., and Ferbey, T. (2017) Magnetite as an indicator mineral in the exploration of porphyry deposits: A case study in till near the Mount Polley Cu-Au deposit, British Columbia, Canada. *Economic Geology and the Bulletin of the Society of Economic Geologists*, 112, 919–940, <https://doi.org/10.2113/econgeo.112.4.919>.
- Prowatke, S. and Klemme, S. (2006) Trace element partitioning between apatite and silicate melts. *Geochimica et Cosmochimica Acta*, 70, 4513–4527, <https://doi.org/10.1016/j.gca.2006.06.162>.
- Qiu, K.F., Yu, H.C., Hetherington, C., Huang, Y.Q., Yang, T., and Deng, J. (2021) Tourmaline composition and boron isotope signature as a tracer of magmatic-hydrothermal processes. *American Mineralogist*, 106, 1033–1044.
- Schönig, J., von Eynatten, H., Tolosana-Delgado, R., and Meinhold, G. (2021) Garnet major-element composition as an indicator of host-rock type: A machine learning approach using the random forest classifier. *Contributions to Mineralogy and Petrology*, 176, 98, <https://doi.org/10.1007/s00410-021-01854-w>.
- Sha, L.K. and Chappell, B.W. (1999) Apatite chemical composition, determined by electron microprobe and laser-ablation inductively coupled plasma mass spectrometry, as a probe into granite petrogenesis. *Geochimica et Cosmochimica Acta*, 63, 3861–3881, [https://doi.org/10.1016/S0016-7037\(99\)00210-0](https://doi.org/10.1016/S0016-7037(99)00210-0).
- Shen, Y., Ruijsch, J., Lu, M., Sutanudjaja, E.H., and Karssenberg, D. (2022) Random forests-based error-correction of streamflow from a large-scale hydrological model: Using model state variables to estimate error terms. *Computers & Geosciences*, 159, 105019, <https://doi.org/10.1016/j.cageo.2021.105019>.
- Sillitoe, R.H. (2010) Porphyry copper systems. *Economic Geology and the Bulletin of the Society of Economic Geologists*, 105, 3–41, <https://doi.org/10.2113/gsecongeo.105.1.3>.
- Snider, L.A. and Swedo, S.E. (2004) PANDAS: Current status and directions for research. *Molecular Psychiatry*, 9, 900–907, <https://doi.org/10.1038/sj.mp.4001542>.
- Snow, C.A. (2006) A reevaluation of tectonic discrimination diagrams and a new probabilistic approach using large geochemical databases: Moving beyond binary and ternary plots. *Journal of Geophysical Research. Solid Earth*, 111, <https://doi.org/10.1029/2005JB003799>.
- Soofi, A.A. and Awan, A. (2017) Classification techniques in machine learning: Applications and issues. *Journal of Basic and Applied Sciences*, 13, 459–465, <https://doi.org/10.6000/1927-5129.2017.13.76>.
- Stock, M.J., Humphreys, M., Smith, V.C., Isaia, R., and Pyle, D.M. (2016) Late-stage volatile saturation as a potential trigger for explosive volcanic eruptions. *Nature Geoscience*, 9, 249–254, <https://doi.org/10.1038/ngeo2639>.
- Sun, J.F., Yang, J.H., Zhang, J.H., Yang, Y.H., and Zhu, Y.S. (2021) Apatite geochemical and SrNd isotopic insights into granitoid petrogenesis. *Chemical Geology*, 566, 120104, <https://doi.org/10.1016/j.chemgeo.2021.120104>.
- Vapnik, V.N. (1995) *The Nature of Statistical Learning Theory*, 188 p. Springer.
- Wang, C., Deng, C., and Wang, S. (2020) Imbalance-XGBoost: Leveraging weighted and focal losses for binary label-imbalanced classification with XGBoost. *Pattern Recognition Letters*, 136, 190–197, <https://doi.org/10.1016/j.patrec.2020.05.035>.
- Wang, Y., Qiu, K.F., Müller, A., Hou, Z.L., Zhu, Z.H., and Yu, H.C. (2021) Machine learning prediction of quartz forming-environments. *Journal of Geophysical Research: Solid Earth*, 126, e2021JB021925.
- Wang, Y., Qiu, K.F., Hou, Z.L., and Yu, H.C. (2022) Quartz Ti/Ge-P discrimination diagram: A machine learning based approach for deposit classification. *Yanshi Xuebao*, 38, 281–290.
- Waskom, M.L. (2021) Seaborn: Statistical data visualization. *Journal of Open Source Software*, 6, 3021, <https://doi.org/10.21105/joss.03021>.
- Xing, K., Shu, Q., and Lentz, D.R. (2021) Constraints on the formation of the giant Daheishan porphyry Mo deposit (NE China) from whole-rock and accessory mineral geochemistry. *Journal of Petrology*, 62, egab018, <https://doi.org/10.1093/petrology/egab018>.
- Yang, J.H., Kang, L.F., Peng, J.T., Zhong, H., Gao, J.F., and Liu, L. (2018) In-situ elemental and isotopic compositions of apatite and zircon from the Shuikoushan and Xihuashan granitic plutons: Implication for Jurassic granitoid-related Cu-Pb-Zn and 646 W mineralization in the Nanling Range, South China. *Ore Geology Reviews*, 93, 647 382–403.
- Yu, H.C., Qiu, K.F., Hetherington, C.J., Chew, D., Huang, Y.Q., He, D.Y., Geng, J.Z., and Xian, H.Y. (2021) Apatite as an alternative petrochronometer to trace the evolution of magmatic systems containing metamict zircon. *Contributions to Mineralogy and Petrology*, 176, 68, <https://doi.org/10.1007/s00410-021-01827-z>.
- Yu, H.C., Qiu, K.F., Chew, D., Yu, C., Ding, Z.J., Zhou, T., Li, S., and Sun, K.F. (2022) Buried Triassic rocks and vertical distribution of ores in the giant Jiaodong gold 650 province (China) revealed by apatite xenocrysts in hydrothermal quartz veins. *Ore 651. Dizhi Lumping*, 140, 104612.
- Zhang, G.L., Wang, S., Zhang, J., Zhan, M.J., and Zhao, Z.H. (2020) Evidence for the essential role of CO₂ in the volcanism of the waning Caroline mantle plume. *Geochimica et Cosmochimica Acta*, 290, 391–407, <https://doi.org/10.1016/j.gca.2020.09.018>.
- Zhong, R., Deng, Y., Li, W., Danyushevsky, L.V., Cracknell, M.J., Belousov, I., Chen, Y.J., and Li, L.M. (2021) Revealing the multi-stage ore-forming history of a mineral deposit using pyrite geochemistry and machine learning-based data interpretation. *Ore Geology Reviews*, 133, 104079, <https://doi.org/10.1016/j.oregeorev.2021.104079>.
- Zhou, R.J., Wen, G., Li, J.W., Jiang, S.Y., Hu, H., Deng, X.D., Zhao, X.F., Yan, D.R., Wei, K.T., Cai, H.A., and others. (2022a) Apatite chemistry as a petrogenetic-metallogenetic indicator for skarn ore-related granitoids: An example from the Daye Fe-Cu-(Au-Mo-W) district, Eastern China. *Contributions to Mineralogy and Petrology*, 177, 23, <https://doi.org/10.1007/s00410-022-01890-0>.
- Zhou, T., Qiu, K.F., Wang, Y., Yu, H.C., and Hou, Z.L. (2022b) Apatite Eu/Y-Ce discrimination diagram: A big data-based approach for provenance classification. *Yanshi Xuebao*, 38, 291–299.

MANUSCRIPT RECEIVED SEPTEMBER 25, 2022

MANUSCRIPT ACCEPTED MARCH 8, 2023

ACCEPTED MANUSCRIPT ONLINE MARCH 16, 2023

MANUSCRIPT HANDLED BY MAURIZIO PETRELLI

Endnote:

¹Deposit item AM-24-28805. Online Materials are free to all readers. Go online, via the table of contents or article view, and find the tab or link for supplemental materials.